



A comparative study of the dynamic fragmentation of non-linear elastic and elasto-plastic rings: The roles of stored elastic energy and plastic dissipation

A. Vaz-Romero, Sébastien Mercier, J.A. Rodríguez-Martínez, Alain Molinari

► To cite this version:

A. Vaz-Romero, Sébastien Mercier, J.A. Rodríguez-Martínez, Alain Molinari. A comparative study of the dynamic fragmentation of non-linear elastic and elasto-plastic rings: The roles of stored elastic energy and plastic dissipation. *Mechanics of Materials*, 2019, 132, pp.134-148. 10.1016/j.mechmat.2019.02.002 . hal-03225386

HAL Id: hal-03225386

<https://hal.univ-lorraine.fr/hal-03225386v1>

Submitted on 22 Oct 2021

HAL is a multi-disciplinary open access archive for the deposit and dissemination of scientific research documents, whether they are published or not. The documents may come from teaching and research institutions in France or abroad, or from public or private research centers.

L'archive ouverte pluridisciplinaire **HAL**, est destinée au dépôt et à la diffusion de documents scientifiques de niveau recherche, publiés ou non, émanant des établissements d'enseignement et de recherche français ou étrangers, des laboratoires publics ou privés.



Distributed under a Creative Commons Attribution - NonCommercial 4.0 International License

A comparative study of the dynamic fragmentation of non-linear elastic and elasto-plastic rings: the roles of stored elastic energy and plastic dissipation

A. Vaz-Romero^a, S. Mercier^b, J. A. Rodríguez-Martínez^{a,b}, A. Molinari^{b,*}

^a*Department of Continuum Mechanics and Structural Analysis. University Carlos III of Madrid. Avda. de la Universidad, 30. 28911 Leganés, Madrid, Spain*

^b*Université de Lorraine, CNRS, Arts et Métiers ParisTech, LEM3, F-57000 Metz, France*

Abstract

We develop a comparative analysis of the processes of dynamic necking and fragmentation in elasto-plastic and hyperelastic ductile rings subjected to rapid radial expansion. For that purpose, finite element simulations have been carried out using the commercial code ABAQUS/Explicit. Expanding velocities which range between 25 *m/s* and 600 *m/s* have been investigated. The elasto-plastic material and the hyperelastic material are modelled with constitutive equations which provide nearly the same stress-strain response during monotonic uniaxial tensile loading, and fracture is assumed to occur at the same level of deformation energy. The computations have revealed that, while the number of necks nucleated in the elasto-plastic and hyperelastic rings is similar, the mechanisms which control their development are significantly different. In the elasto-plastic rings several necks are arrested due to the stress waves which travel the specimen after the localization process has started, and thus the number of fractures in the ring is significantly lower than the number of incepted necks. On the contrary, these stress waves do not stop the development of any neck in the hyperelastic rings. The elastic energy released from the sections of the ring which are unloading during the localization process fuels the development of the necks. Hence, for the whole range of investigated velocities, the proportion of necks that develop into fracture sites is much greater for the hyperelastic rings than for the elasto-plastic ones. The comparison between the numerical results obtained for both materials brings to light the roles of elastic unloading and plastic dissipation in multiple necking and fragmentation processes.

Keywords:

Dynamic necking, Fragmentation, Numerical simulations, Plasticity, Hyperelasticity

1. Introduction

The mechanics of multiple necking and fragmentation in ductile metals submitted to high strain rates have been a subject of investigation over the last 70 years. The theoretical framework developed by Mott (1947),

*Corresponding author. Tel. +33 387315369; Fax: +33 387315366. E-mail address: alain.molinari@univ-lorraine.fr

which aimed to describe the process of fragmentation resulting from the explosive rupture of cylindrical casings, was the first attempt to identify the mechanisms which control multiple fracture in metallic structures. The theory of Mott describes the onset of fractures as random processes that respond to the inherent variability in the fracture strain of ductile materials. When fracture occurs at one point, stress waves (named as Mott's waves) propagate away from the fracture sites releasing the stress in the neighbourhood. Within the regions of the specimen subjected to the action of the release waves, the material does not continue to stretch and thus failure is precluded. The size of the fragments is then determined by the distance travelled by the release wave. However, an assumption of Mott's theory is that fractures occur instantaneously and thus the fracture energy was not accounted for. Nevertheless, the proposed theory was able to predict the distributions of fragment sizes observed in the fragmentation of plastically deforming casings.

Grady and co-workers (Grady et al., 1984; Kipp and Grady, 1985; Grady, 2002) enhanced the theory of Mott by including the dissipation of energy associated with the fracture process. Grady (2006) argued that *some degree of work must be expended, and some fracture energy overcome, in opening the cracks delineating the fragment boundaries produced in the fragmentation event.* In this way, the stress release analysis developed by Mott (1947) was extended by considering the time history of plastic release waves emanating from sites of fracture. These authors were able to predict the average fragment size observed in experiments, and showed that the fracture energy scales the fragment size.

Over the last two decades, the ideas of Mott (1947) and Grady and co-workers (Grady et al., 1984; Kipp and Grady, 1985; Grady, 2002) have been frequently applied to interpret and model the distributions of necks and fragment sizes observed in ring expansion experiments. The ring expansion test, originally developed by Niordson (1965), consists of an electromagnetic device which drives the radial expansion of a thin ring at velocities as large as 300 m/s . The success of this experiment lies in the radial symmetry of specimen and loading conditions. This symmetry practically eliminates the propagation of stress waves along the hoop direction of the sample before localization, and allows to reveal the true dynamic properties of the material.

Grady and Olsen (2003) performed experiments on rings of uranium-6%-niobium (U6N) with 30 mm in diameter, and square cross section with 0.75 mm in thickness. The expanding velocities covered during the experiments ranged between 50 m/s and 300 m/s . More recently, Ravi-Chandar and co-workers (Zhang and Ravi-Chandar, 2006, 2008; Cliche and Ravi-Chandar, 2018), carried out experiments with specimens made of Al 6060-O, Al 1100-H14, Cu-101 and AZ31B-O, for expanding velocities which ranged between 40 m/s and 225 m/s . The thickness of the samples was 0.5 mm , their cross-sectional length was varied from 0.5 mm to 2.286 mm , and their diameter from 30 mm to 33 mm . In all these works, the formation of fragments

was analysed using Mott's and Grady's probabilistic models for fragmentation. The authors stated that the fragmentation which follows the formation of multiple necks in ductile metallic rings can be described in terms of the Mott's release waves.

To gain additional insight into these experimental results, Ravi-Chandar and Triantafyllidis (2015) developed a 1D finite difference model to simulate incompressible non-linear elastic bars subjected to dynamic stretching. Localized perturbations of strain and velocity were included in the bars at different locations. The authors suggested that the distance between necks, and thus the size of the fragments in the subsequent fragmentation process, is influenced by the interaction between these perturbations that travel along the bar as the loading time evolves. This idea finds resemblance with the theory of Mott who, as mentioned before, assumed that the distribution of fractures responds to the inevitable imperfections present in all materials. However, the numerical calculations of Ravi-Chandar and Triantafyllidis (2015), being based on the method of characteristics, were restricted to strains below the one obtained from the Considère criterion. Since loading conditions prevailed at all points of the bar during the calculations, it was not possible to investigate the role of unloading waves in the development of the necking pattern. In order to complement the computations of Ravi-Chandar and Triantafyllidis (2015), Vaz-Romero et al. (2017) carried out 3D finite element simulations in ABAQUS/Explicit of non-linear elastic rods subjected to dynamic stretching. In the simulations of Vaz-Romero et al. (2017), the strains attained in the bars were above the one obtained from the Considère criterion. It was shown that, due to inertia effects, the core of the multiple necking process occurs during the post-uniform deformation regime of the bar. Note that, for elasto-plastic materials under dynamic loading, the role of inertia in the formation of the multiple necking pattern during the post-Considère regime has been elucidated in various aspects by theoretical stability analyses, see the works of Fressengeas and Molinari (1994), Mercier and Molinari (2003, 2004), Zhou et al. (2006), Xue et al. (2008), Rodríguez-Martínez et al. (2013a, 2015) and El Maï et al. (2014). The importance of accounting for elastic unloading in order to simulate the formation and development of the necking pattern was also noted by Vaz-Romero et al. (2017), who made clear that their results were *specific for non-linear elastic bars and, in principle, could not be extrapolated to elasto-plastic specimens*.

Motivated by this statement of Vaz-Romero et al. (2017), in the present paper we carry out finite element simulations using ABAQUS/Explicit (2013) of elasto-plastic and hyperelastic rings subjected to dynamic expansion at velocities varying from 25 m/s to 600 m/s . The elasto-plastic material and the hyperelastic material are modelled with constitutive equations which provide nearly the same stress-strain response during monotonic uniaxial tensile loading. The simulations conducted for both materials bring to light the influence of

plastic dissipation and elastic unloading in the development of the necking pattern, and provides new insights into the role of the release waves that emanate from nucleated necks and fracture sites in the fragmentation of elasto-plastic and hyperelastic specimens.

2. Constitutive frameworks

Two different isotropic constitutive frameworks are used to model the mechanical behaviour of the material in ring expansion simulations: (1) an elasto-plastic model and (2) a hyperelastic model. Both constitutive models are laid out in order to provide nearly the same stress-strain response during loading. The difference sets in the unloading process, as further shown in Sections 2.1 and 2.2. The objective of the present work is to provide a deeper understanding on the respective effects on necking and fragmentation of (i) plastic dissipation (elasto-plastic case) and (ii) stored and released elastic energy (hyperelastic case).

2.1. Elasto-plastic constitutive model

The constitutive model, pre-implemented in ABAQUS/Explicit (2013), follows the standard principles of von Mises plasticity. The strain rate tensor \mathbf{d} is decomposed as the sum of an elastic \mathbf{d}^e and a plastic part \mathbf{d}^p :

$$\mathbf{d} = \mathbf{d}^e + \mathbf{d}^p \quad (1)$$

The relation between the elastic strain rate and the stress rate is given by the following hypo-elastic law:

$$\dot{\boldsymbol{\sigma}} = \mathbf{C} : \mathbf{d}^e \quad (2)$$

where $\dot{\boldsymbol{\sigma}}$ is the Green-Naghdi objective derivative of the Cauchy stress tensor and \mathbf{C} is the tensor of isotropic elastic moduli given by:

$$\mathbf{C} = 2G\tilde{\mathbf{I}} + K\mathbf{1} \otimes \mathbf{1} \quad (3)$$

where G is the elastic shear modulus, K is the bulk modulus, $\mathbf{1}$ is the second order unit tensor and $\tilde{\mathbf{I}}$ is the fourth order deviatoric unit tensor.

Moreover, the plastic part of the strain rate tensor is defined by the J_2 flow law:

$$\mathbf{d}^p = \frac{3}{2} \dot{\bar{\varepsilon}}^p \frac{\mathbf{s}}{\bar{\sigma}} \quad (4)$$

where $\dot{\bar{\varepsilon}}^p = \sqrt{\frac{2}{3} \mathbf{d}^p : \mathbf{d}^p}$ is the equivalent plastic strain rate and $\bar{\sigma} = \sqrt{\frac{3}{2} \mathbf{s} : \mathbf{s}}$ is the equivalent von Mises stress. Moreover, $\mathbf{s} = \boldsymbol{\sigma} - \sigma_h \mathbf{1}$ denotes the deviatoric Cauchy stress tensor and $\sigma_h = \frac{1}{3} \boldsymbol{\sigma} : \mathbf{1}$ is the mean stress. The yield function f is given by:

$$f = \bar{\sigma} - \sigma_y \quad (5)$$

where σ_y is the yield stress of the material defined as:

$$\sigma_y = B (\bar{\varepsilon}^p + \varepsilon_0)^n \quad (6)$$

where B , ε_0 and n are material constants and $\bar{\varepsilon}^p = \int_0^t \dot{\bar{\varepsilon}}^p(\tau) d\tau$ is the accumulated plastic strain.

Thermal and viscous effects are not considered in the constitutive behaviour of the material so that the effects of inertia, stress multiaxiality and strain hardening control the formation of necks in the ring. On the one hand, we are aware that thermal and viscous effects may be important in the behaviour of elasto-plastic materials subjected to high strain rates. On the other hand, note that similar constitutive model was used by Zhang and Ravi-Chandar (2010) to investigate the mechanisms of dynamic fragmentation in metallic tubes subjected to rapid radial expansion. In addition, neglecting thermal and viscous effects allows to identify, by comparison with the results obtained with the non-linear elastic material presented in section 2.2, the specific roles of plastic dissipation, stored elastic energy and unloading waves in the necking and fragmentation behaviors of ductile rings subjected to high velocity radial expansion. Moreover, note that, during unloading, the response of the elasto-plastic material is given by the linear elastic law defined by Eq. (2), see Fig. 1.

2.2. Hyperelastic constitutive model

The goal is to model a non-linear elastic material which, under monotonic uniaxial tensile loading, replicates the response of the elasto-plastic material described in Section 2.1. Following Ogden (1997), we use the isochoric-volumetric decomposition of the strain energy density:

$$\Psi(\tilde{I}_1, J) = \Psi_{iso}(\tilde{I}_1) + \Psi_{vol}(J) \quad (7)$$

where \tilde{I}_1 is the first invariant of the isochoric left Cauchy-Green strain tensor $\tilde{\mathbf{b}} = J^{-2/3} \mathbf{F} \mathbf{F}^T$, where \mathbf{F} is the deformation gradient tensor and J is the determinant of \mathbf{F} .

The Cauchy stress tensor is then given by the hyperelastic constitutive relation:

$$\boldsymbol{\sigma} = \frac{1}{J} \frac{\partial \Psi(\tilde{I}_1, J)}{\partial \mathbf{F}} \mathbf{F}^T \quad (8)$$

which leads to (e.g. Bergstrom (2015)):

$$\boldsymbol{\sigma} = \boldsymbol{\sigma}^{iso} + \boldsymbol{\sigma}^{vol} = \frac{2}{J} \frac{\partial \Psi_{iso}(\tilde{I}_1)}{\partial \tilde{I}_1} \tilde{\mathbf{b}}^* + K (J - 1) \mathbf{1} \quad (9)$$

where we have assumed, following for instance Bergstrom (2015), that $\Psi_{vol}(J) = \frac{K}{2} (J - 1)^2$. Moreover, note that $\tilde{\mathbf{b}}^* = \tilde{\mathbf{b}} - \frac{1}{3} \tilde{I}_1 \mathbf{1}$. Recall that K is the bulk modulus.

As shown by Gough et al. (1999) and Marlow (2003), since $\Psi_{iso}(\tilde{I}_1)$ depends exclusively on the invariant \tilde{I}_1 , the isochoric strain energy can be completely determined from a single mechanical test. Thus, let us consider a uniaxial tension test defined by the following deformation gradient tensor:

$$\mathbf{F} = \begin{bmatrix} \lambda_1 & 0 & 0 \\ 0 & \lambda_2 & 0 \\ 0 & 0 & \lambda_3 \end{bmatrix} \quad (10)$$

where λ_1 is the stretch in the direction of loading and $\lambda_2 = \lambda_3$ are the stretches in the perpendicular directions. The component of the stress in the direction of the loading is recorded so that a relation exists between σ_{11} and the longitudinal stretch λ_1 or, equivalently, between σ_{11} and $\ln(\lambda_1)$:

$$\sigma_{11} = H(\ln(\lambda_1)) \quad (11)$$

As an example, for a material with Norton type behavior, the function H is of the form $H(x) = B(x + x_o)^n$. The isochoric left Cauchy-Green tensor is:

$$\tilde{\mathbf{b}} = \begin{bmatrix} \tilde{\lambda}_1^2 & 0 & 0 \\ 0 & \tilde{\lambda}_2^2 & 0 \\ 0 & 0 & \tilde{\lambda}_2^2 \end{bmatrix} \quad (12)$$

where $\tilde{\lambda}_1^2 = J^{-2/3}\lambda_1^2$ and $\tilde{\lambda}_2^2 = J^{-2/3}\lambda_2^2$. Since $\det \tilde{\mathbf{b}} = 1$, we have that $\tilde{\lambda}_2 = \tilde{\lambda}_1^{-1/2}$, and therefore the first invariant of $\tilde{\mathbf{b}}$ is:

$$\tilde{I}_1 = \tilde{\lambda}_1^2 + 2\tilde{\lambda}_1^{-1} \quad (13)$$

Hence, the tensor $\tilde{\mathbf{b}}^*$ is defined as:

$$\tilde{\mathbf{b}}^* = \begin{bmatrix} \frac{2}{3}(\tilde{\lambda}_1^2 - \tilde{\lambda}_1^{-1}) & 0 & 0 \\ 0 & -\frac{1}{3}(\tilde{\lambda}_1^2 - \tilde{\lambda}_1^{-1}) & 0 \\ 0 & 0 & -\frac{1}{3}(\tilde{\lambda}_1^2 - \tilde{\lambda}_1^{-1}) \end{bmatrix} \quad (14)$$

Therefore, under uniaxial tension conditions (assuming that the stress state in the specimen is homogeneous), the components of the Cauchy stress tensor in the loading and perpendicular directions, based on Eq. (9), are obtained:

$$\sigma_{11} = \frac{4}{3J} \frac{\partial \Psi_{iso}(\tilde{I}_1)}{\partial \tilde{I}_1} (\tilde{\lambda}_1^2 - \tilde{\lambda}_1^{-1}) + K(J-1) \quad (15)$$

$$\sigma_{22} = \sigma_{33} = \frac{-2}{3J} \frac{\partial \Psi_{iso}(\tilde{I}_1)}{\partial \tilde{I}_1} (\tilde{\lambda}_1^2 - \tilde{\lambda}_1^{-1}) + K(J-1) \quad (16)$$

For a uniaxial tension test, the lateral surface of the specimen is traction free, which implies that $\sigma_{22} = \sigma_{33} = 0$. Thus, from Eq. (16) we have:

$$K(J-1) = \frac{2}{3J} \frac{\partial \Psi_{iso}(\tilde{I}_1)}{\partial \tilde{I}_1} (\tilde{\lambda}_1^2 - \tilde{\lambda}_1^{-1}) \quad (17)$$

Using Eqs. (15) and (17), the component of the Cauchy stress tensor in the loading direction becomes:

$$\sigma_{11} = \frac{2}{J} \frac{\partial \Psi_{iso}(\tilde{I}_1)}{\partial \tilde{I}_1} (\tilde{\lambda}_1^2 - \tilde{\lambda}_1^{-1}) \quad (18)$$

For any material subjected to uniaxial tension, all the variables of the problem can be expressed in terms

of the longitudinal stretch λ_1 or, analogously, of $\ln(\lambda_1)$. Therefore, the Jacobian can be expressed as $J(\ln(\lambda_1))$. This allows to obtain a relationship between the longitudinal stretch λ_1 and the isochoric longitudinal stretch $\tilde{\lambda}_1$ such that $\lambda_1 = \kappa(\tilde{\lambda}_1)$ with $\kappa^{-1}(\lambda_1) = \{J(\ln(\lambda_1))\}^{-\frac{1}{3}}\lambda_1$. Therefore, knowing the tensile response of the hyperelastic material Eq. (11), it is possible to obtain a relationship between σ_{11} and $\tilde{\lambda}_1$:

$$\sigma_{11} = H(\ln(\lambda_1)) = F(\ln(\tilde{\lambda}_1)) \quad (19)$$

Note that, if the material is incompressible, the functions H and F are identical since $J = 1$ and therefore $\tilde{\lambda}_1 = \lambda_1$. It follows from the equation (18) that the derivative of the isochoric part of the strain energy is solely depending upon the tensile response of the material, as proposed by Marlow (2003).

$$\frac{\partial \Psi_{iso}(\tilde{I}_1)}{\partial \tilde{I}_1} = \frac{J}{2} \left[\frac{F(\ln(\tilde{\lambda}_1))}{\tilde{\lambda}_1^2 - \tilde{\lambda}_1^{-1}} \right] \quad (20)$$

Previous expression shows that the derivative of the isochoric strain energy is related to $\tilde{\lambda}_1$. Nevertheless, from equation (13), a link between $\tilde{\lambda}_1$ and \tilde{I}_1 can be obtained through a third-order polynomial equation in $\tilde{\lambda}_1$:

$$\tilde{\lambda}_1^3 - \tilde{I}_1 \tilde{\lambda}_1 + 2 = 0 \quad (21)$$

Indeed, based on the Cardano's formula, only one root is real and two are imaginary. The real root is the physical solution:

$$\tilde{\lambda}_1 = \frac{3^{1/3} \tilde{I}_1 + \left(-9 + \sqrt{81 - 3\tilde{I}_1^3} \right)^{2/3}}{3^{2/3} \left(-9 + \sqrt{81 - 3\tilde{I}_1^3} \right)^{1/3}} \quad (22)$$

Therefore, inserting (22) into (20) proves that the derivative of the isochoric strain energy has an explicit expression which is related to the first invariant \tilde{I}_1 , and to the uniaxial stress-strain response of the hyperelastic material given by the function $F(\ln(\tilde{\lambda}_1))$. Finally Eqs. (9), (20) and (22) provide the expression of the Cauchy stress tensor for the considered hyperelastic material:

$$\boldsymbol{\sigma} = \frac{F(\ln(\tilde{\lambda}_1(\tilde{I}_1)))}{\left(\tilde{\lambda}_1(\tilde{I}_1) \right)^2 - \left(\tilde{\lambda}_1(\tilde{I}_1) \right)^{-1}} \tilde{\mathbf{b}}^*(\tilde{I}_1) + K(J-1) \mathbf{1} \quad (23)$$

with $\tilde{\lambda}_1(\tilde{I}_1)$ given by equation (22). Therefore, the general form of the constitutive law has been identified from a single tensile test. The hyperelastic constitutive model, Eq. (23), has been implemented in

ABAQUS/Explicit (2013) through a VUMAT subroutine.

In order to have the same loading response for the elasto-plastic and the hyperelastic materials, Eq. (6) is used with $\varepsilon_0 = 0$ for the hyperelastic material (i.e. $F(\ln(\tilde{\lambda}_1)) = B \ln(\tilde{\lambda}_1)^n$) and $\varepsilon_0 = 0.0001$ for the elasto-plastic material. Thus, the initial yield stress of the elasto-plastic material is 263 MPa , see Fig. 1. Other material parameters, which are taken from the works of Ravi-Chandar and Triantafyllidis (2015) and Vaz-Romero et al. (2017), are provided in Table 1. As mentioned before, the material is considered nearly incompressible. The value of K reported in Table 1 corresponds to a Poisson's ratio of 0.495.

Symbol	Property and units	Value
ρ_0	Initial density (kg/m^3)	7740
G	Elastic shear modulus (GPa)	87.9
K	Bulk modulus (GPa)	8766
B	Material parameter (GPa)	2
ε_0	Material parameter	0.0001
n	Material parameter	0.22

Table 1: Values of the parameters used in the elasto-plastic and hyperelastic constitutive models.

Fig. 1 compares loading and unloading stress-strain curves obtained from both constitutive models under uniaxial tension. Note that $\varepsilon_{11} = \ln(\lambda_1)$ is the logarithmic strain. The loading $\sigma_{11} - \varepsilon_{11}$ curves are superimposed, also for strains greater than the one obtained from the Considère criterion (0.22 for this material), see Fig. 1. This is important for dynamic applications in which, due to the stabilizing effect of inertia, the necking pattern is formed during the post-Considère deformation regime, see for instance the work of Vaz-Romero et al. (2017). As mentioned before, neglecting the strain rate and temperature dependencies of both materials facilitates to obtain good agreement between their respective loading curves, which is required to identify the specific roles of elastic stored energy and plastic dissipation in the necking and fragmentation behaviours of non-linear elastic and elasto-plastic rings. The only difference between the loading curves, that can hardly be noticed in the figure, even in the zoomed area shown in the left bottom part of Fig. 1, occurs below the initial yield stress of the elasto-plastic material when it features a linear stress-strain response, see Eq. (2), while the hyper-elastic material already features a non-linear behaviour. Nevertheless, we assume that this difference in the response of both materials under monotonic uniaxial tensile loading is not playing any significant role in the results presented in Section 4. On the other hand, as mentioned before, the unloading $\sigma_{11} - \varepsilon_{11}$ curves are very different, see the arrows depicted in Fig. 1. For the elasto-plastic material, the stress goes to zero following

the linear elastic law defined by Eq. (2). For the hyperelastic material, the stress goes to zero following the path taken during loading.

Moreover, we are aware that non-linear elastic materials (e.g. some polymers) do not feature, under uniaxial tension, the concave-downward shape shown in Fig. 1. In many of these materials the nominal stress under uniaxial tension is an increasing function of the strain, see Treolar (1944). Thus the Considère criterion is never fulfilled, which precludes the formation of necks. In some others, the nominal stress first presents a peak, then drops until reaching a minimum, and then increases again to levels well above the initial peak. As shown by Hutchinson and Neale (1983), a neck initiates in these materials in the same way as in the materials presented in Fig. 1. However, the upturn of the uniaxial stress-strain curve forces the neck to spread along the entire size of the specimen, instead of remaining localized as in the materials presented in Fig. 1 which are described by a power-law, see equation (6). Therefore, the non-linear elastic material used in this work should be understood as a model material that, by comparison with the elasto-plastic material, allows to provide new insights into the role of elastic unloading on the formation of multiple necking and fragmentation patterns in ductile metals. [Note that Ravi-Chandar and Triantafyllidis \(2015\) used similar constitutive model to investigate the necking and fragmentation behaviours of metallic rings subjected to rapid radial expansion.](#)

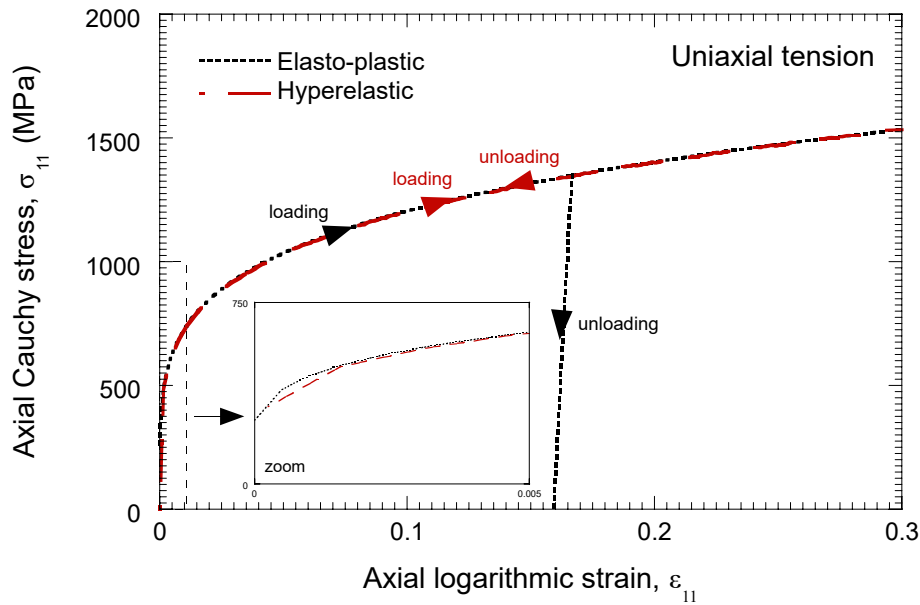


Figure 1: Axial Cauchy stress σ_{11} versus axial logarithmic strain ε_{11} for the elasto-plastic material and the hyperelastic material. While the loading path is almost identical for both materials, elastic unloading is different, see the arrows included in the plot. [A zoom illustrating response of the material for low values of \$\varepsilon_{11}\$ is included in the left bottom part of the plot.](#)

3. Finite element model

A 3D finite element model has been developed in ABAQUS/Explicit (2013) to simulate multiple necking and fragmentation in ductile rings subjected to rapid radial expansion. The numerical model, shown in Fig. 2, is based on previous works (Becker, 2002; Rusinek and Zaera, 2007; Vadillo et al., 2012; Rodríguez-Martínez et al., 2013b,a). Let $\{R, \Theta, Z\}$ denote the cylindrical Lagrangian coordinates of a point in the ring in the undeformed state, and $\{r, \theta, z\}$ the current position at time t , see Fig. 2. The initial thickness of the square cross section of the ring is $e_0 = 0.75 \text{ mm}$, and its initial inner and outer radii are $R_i = 15 \text{ mm}$ and $R_o = 15.75 \text{ mm}$, respectively. These dimensions are taken from Rodríguez-Martínez et al. (2013a), and are similar to those used in the experiments of Grady and Olsen (2003) and Zhang and Ravi-Chandar (2006, 2008). The boundary and initial conditions applied in the simulations are:

- **Boundary conditions:** the following velocity boundary condition has been applied to the inner surface of the ring.

$$V_R(R_i, \Theta, Z, t) = V$$

where V_R is the radial particle velocity. The outer and lateral surfaces of the ring are traction free.

- **Initial conditions.** The specimen is initially undeformed and unstressed. An initial velocity field is prescribed to all material points.

$$V_R(R, \Theta, Z, 0) = V \sqrt{\frac{R_i}{R}}; \quad V_\Theta(R, \Theta, Z, 0) = 0; \quad V_Z(R, \Theta, Z, 0) = -\frac{V}{2} \sqrt{\frac{R_i}{R^3}} Z$$

where V_Θ and V_Z are the material particle velocities along the circumferential and axial directions, respectively. This velocity field is calculated assuming material incompressibility (which is an approximation for the nearly incompressible materials used in the calculations). Note that, the above initial velocity field is included to avoid, at the initial time, a velocity jump at the boundary that would be conducive to parasite wave propagation effects affecting the localization pattern, (Needleman, 1991; Xue et al., 2008).

The ring is meshed with 63680 eight-node tri-linear brick elements with reduced integration (C3D8R in ABAQUS notation). [The reduced integration helps to prevent mesh locking and provides accurate solutions](#)

in nearly or fully incompressible materials. All the calculations presented in this paper are performed with 1 processor (no parallelization). The mesh shows radial symmetry. Five elements are placed through the thickness of the specimen. The aspect ratio of the elements is close to 1 : 1 : 1 (with dimensions $\approx 0.15 \times 0.15 \times 0.15 \text{ mm}^3$), see Fig. 2. The integral viscoelastic approach available in ABAQUS/Explicit (2013) has been used to prevent hourglass deformation modes, with the scale factor used for all hourglass stiffnesses being equal to one. Neither geometrical nor material imperfections were introduced in the finite element model. The numerical perturbations introduced by the software are sufficient to perturb the field variables, breaking the symmetry of the problem and thus allowing for flow localization (Rusinek and Zaera, 2007; Vadillo et al., 2012). It was discussed in the works of Rodríguez-Martínez et al. (2013a,b, 2017) and Vaz-Romero et al. (2017) that, while the numerical perturbations are not controlled by the user, at high strain rates they do not dictate the average distance between necks but they just allow for the localization to occur. It was shown that the localization pattern obtained in ABAQUS/Explicit calculations, in non-linear elastic and elasto-plastic materials, is controlled, to a large extent, by the constitutive behaviour of the material, inertia effects and stress multiaxiality. Moreover, we have also checked that the numerical perturbations have small influence in the fragmentation results reported in this paper. In fact, we performed simulations with different versions of ABAQUS/Explicit (versions corresponding to different years) and different number of processors (from 1 to 6), and the number of necks and fragments generally varied less than $\approx 5\%$. The loading times corresponding to the beginning and end of the fragmentation process also showed a maximum variation of $\approx 5\% - 7\%$. These results suggest that the trends shown in this paper represent the intrinsic material behavior, and that the inherent variability associated to the numerical calculations (numerical integration, discretization, parallelization, etc.) plays a secondary role.

Material failure is accounted for in the simulations using the element deletion technique available in ABAQUS/Explicit (2013). For the elasto-plastic material, we consider that failure occurs when a critical value of the accumulated plastic strain, denoted by $\bar{\varepsilon}_f$, is reached. Neglecting the contribution of the elastic strains, the mechanical energy per unit volume expended in the deformation of the elasto-plastic material until failure is $E_f^{ep} = \int_0^{\bar{\varepsilon}_f} \bar{\sigma} d\bar{\varepsilon}^p$. Based on equations (5) and (6), the failure energy is:

$$E_f^{ep} = \frac{B}{n+1} [(\bar{\varepsilon}_f + \varepsilon_0)^{n+1} - (\varepsilon_0)^{n+1}] \quad (24)$$

For the hyperelastic material, we consider that failure occurs when the value of the strain energy function $\Psi(\tilde{I}_1, J)$ equals E_f^{ep} , where $\Psi(\tilde{I}_1, J)$ can be obtained after integration of equation (20) using equation (22).

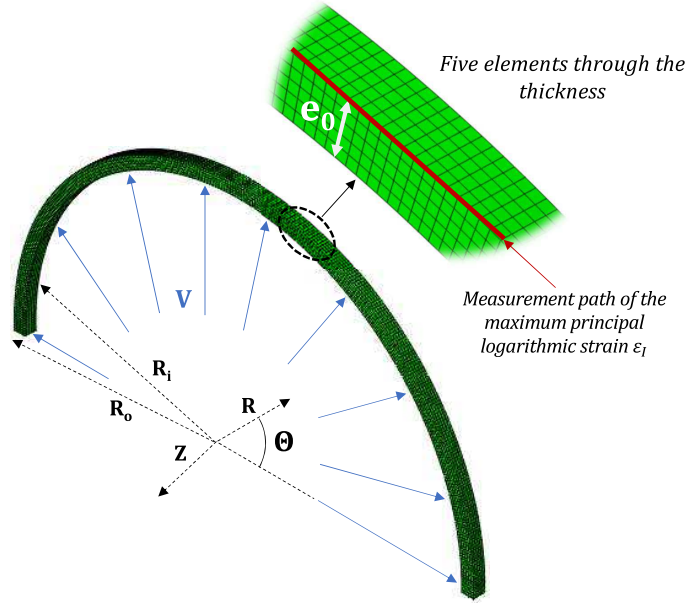


Figure 2: Finite element model. Mesh, geometry and boundary conditions. While only half of the specimen is shown for the sake of clarity, calculations are performed using a model of the whole ring.

Considering that both materials fail for the same level of the deformation energy is a strong assumption. Nevertheless this allows us to compare, on energy basis, the fragmentation behaviour of a ring for an elasto-plastic material and a hyperelastic model material. Note that, while E_f^{ep} and $\Psi(\tilde{I}_1, J)$ are energies per unit volume in the deformed and undeformed configurations, respectively, they can be compared because the materials are considered nearly incompressible.

4. Results

In this Section we [report](#) numerical results obtained with the finite element model [presented](#) in Section 3, and the two constitutive models developed in Section 2. Applied velocities which range between 25 m/s and 600 m/s are investigated. These velocities correspond to initial strain rates ranging from 1666.67 s^{-1} to 40000 s^{-1} . While the largest velocities (and associated strain rates) exceed the regular experimental capabilities (ring expansion tests can rarely be performed for velocities higher than 300 m/s, see Grady and Olsen (2003) and Zhang and Ravi-Chandar (2006, 2008)), exploring such a wide range of loading rates helps to enlighten the differences between the necking and fragmentation behaviours of elasto-plastic and hyperelastic materials. [Recall that the objective of this paper is to shed light into the specific roles played by plastic dissipation, stored elastic energy and unloading waves.](#)

Fig. 3 shows the normalized maximum principal logarithmic strain $\hat{\varepsilon}_I$ versus the normalized angular position $\bar{P} = \frac{\Theta}{2\pi}$ for the two materials. The normalized strain is defined as $\hat{\varepsilon}_I = \frac{\varepsilon_I}{\varepsilon^b}$, where ε_I is the maximum principal logarithmic strain measured along the path shown in Fig. 2. Moreover, $\varepsilon^b = \ln\left(\frac{R_o + Vt}{R_o}\right)$ approximates the background logarithmic strain in the outer surface of the ring (in absence of strain localization). Therefore, during the homogeneous deformation of the specimen, before the localization pattern is formed, the normalized maximum principal logarithmic strain is $\hat{\varepsilon}_I \approx 1$. The $\hat{\varepsilon}_I - \bar{P}$ curves show a succession of peaks and valleys, exposing the multiple necking process which develops in the rings. For the sake of clarity, we only cover values of \bar{P} ranging from 0 to 0.3, i.e. we show results for an angular section of 108° . *Showing 30% of the perimeter of the ring allows to include enough necks to obtain a representative sample of the entire localization pattern, without impairing the clarity of the graph, for all the expansion velocities investigated.*

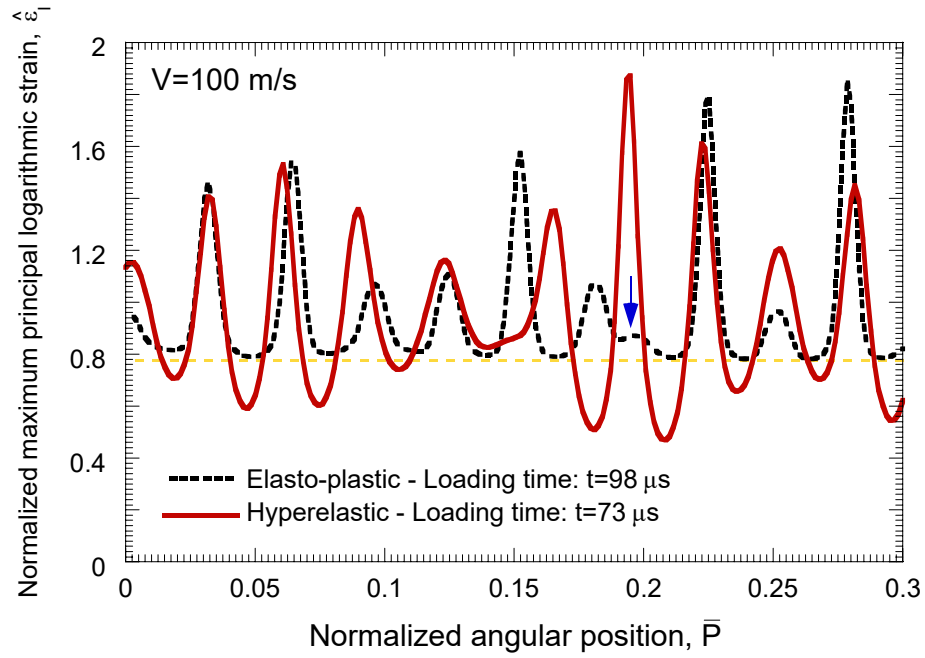
In Fig. 3(a) results are *displayed* for $V = 100 \text{ m/s}$. For the elasto-plastic material they correspond to $t = 98 \text{ } \mu\text{s}$, and for the hyperelastic material to $t = 73 \text{ } \mu\text{s}$. The loading times are selected such that the maximum value of $\hat{\varepsilon}_I$ reaches ≈ 1.9 . This value has been chosen such that the necking pattern is fully formed, yet the strains are not so large that the finite element grid becomes significantly distorted. We consider that a neck is formed when, for a given excursion of strain, the ratio between the peak and the neighbouring valleys is greater than 1.1. The same criterion was used, for instance, in N'souglo et al. (2018). Strain excursions occur in the sections of the ring which develop a strain *significantly larger* than the neighbourhood. The total number of necks in a calculation is determined once the localization pattern is fully developed i.e. further increase in strain does not lead to the formation of new necks. Based on this criterion, in Fig. 3(a) both the elasto-plastic and the hyperelastic ring show 10 necks within the range of \bar{P} investigated. Nevertheless, the formation and development of the necking pattern is different depending on the material type considered. The condition $\hat{\varepsilon}_I \approx 1.9$ is reached earlier in the hyperelastic ring: the development of the necking pattern appears to be faster for the hyperelastic material. In the case of the elasto-plastic ring, one excursion in strain, indicated with a blue arrow in Fig. 3(a), has been arrested before forming a neck (the ratio of strains between the peak and the neighbouring valleys is smaller than 1.1). The strain corresponding to the valleys which surround the excursions is nearly the same for all valleys, i.e. largely independent of the degree of development of the excursions to which they surround. This is indicated with a dashed yellow line which represents the accumulated plastic strain (background plastic strain) prior to full necking localization. In the case of the hyperelastic ring all the excursions in strain reach the neck criterion, none of them is arrested before. Moreover, the more developed is the excursion in strain, the smaller is the strain in the neighbouring valleys (note that for the hyperelastic material the unloading process only ends when the strain reaches zero). This is because the elastic energy

released from the valleys fuels the development of the necks. This idea will be further elaborated when the results of Figs. 4 and 5 will be discussed.

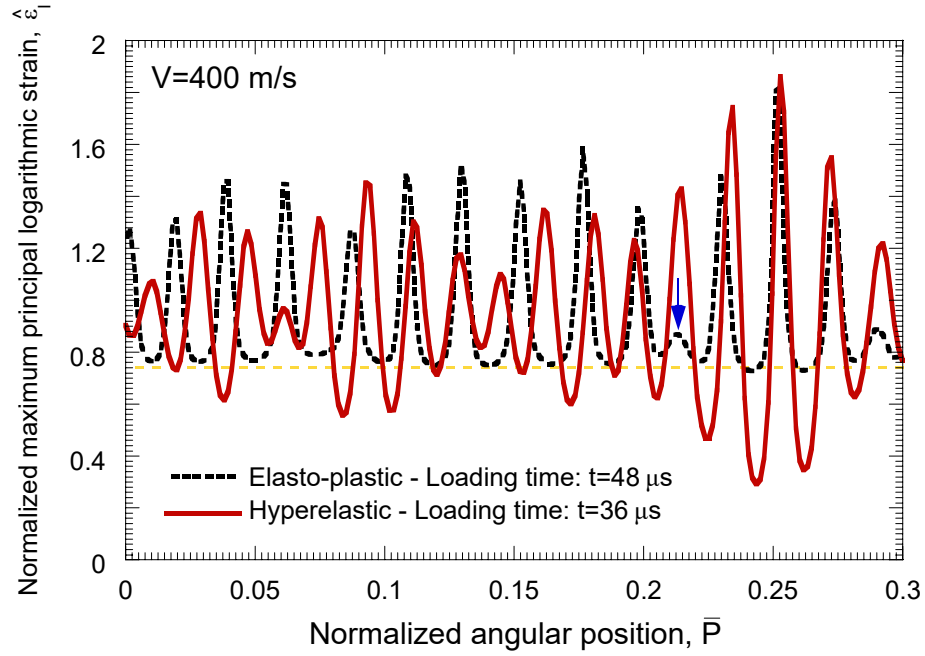
In Fig. 3(b) the applied velocity is four times greater $V = 400 \text{ m/s}$. For the elasto-plastic material the results correspond to $t = 48 \mu\text{s}$, and for the hyperelastic material to $t = 36 \mu\text{s}$. These loading times are selected such that, based on the criterion used in Fig. 3(a), the maximum value of $\hat{\varepsilon}_I$ is ≈ 1.9 . In agreement with the results presented in Fig. 3(a), the necking pattern develops faster for the hyperelastic material. In the case of the elasto-plastic material there are 15 excursions in strain, one of them, indicated with a blue arrow, is arrested before the necking criterion is reached. In the case of the hyperelastic material, there are 17 excursions in strain, all of them reaching the neck criterion. These results suggest that for the hyperelastic material the necking pattern grows faster and all the excursions in strain develop into necks.

Fig. 4 shows the normalized maximum principal logarithmic strain $\hat{\varepsilon}_I$ versus the normalized angular position \bar{P} for both materials investigated and different loading times. The idea is to complement the results presented in Fig. 3, and explore the temporal evolution of the localization pattern. The applied velocity is $V = 100 \text{ m/s}$.

Fig. 4(a) shows results for the elasto-plastic material and three loading times: $t = 88 \mu\text{s}$, $t = 93 \mu\text{s}$ and $t = 98 \mu\text{s}$. Note that the data corresponding to $t = 98 \mu\text{s}$ were already shown in Fig. 3(a). The localization pattern is clearly visible for the three loading times considered. Note that the three $\hat{\varepsilon}_I - \bar{P}$ curves intersect with each other several times. If the $\hat{\varepsilon}_I - \bar{P}$ curve is shifted upwards with increasing time (e.g. the solid red curve $t = 93 \mu\text{s}$ is above the dashed black curve $t = 88 \mu\text{s}$), the maximum principal logarithmic strain ε_I has increased more than the background strain ε^b , which indicates an on-going strain localization process. Similarly, if increasing the loading time shifts the $\hat{\varepsilon}_I - \bar{P}$ curve downwards (e.g. the solid red curve is below the dashed black curve), the material is unloading elastically. Thus, we observe that all the valleys which surround the excursions in strain are being unloaded within the time interval $88 - 98 \mu\text{s}$: the dashed green curve is below the solid red curve and this red curve, in turn, is below the dashed black curve. The value of $\hat{\varepsilon}_I$ is nearly the same for all valleys for each time investigated (as mentioned before). This value is determined by the accumulated plastic strain in the material prior to full necking localization (which remains constant while ε^b increases with loading time). On the other hand, some of the excursions in strain progress during the time interval $88 - 98 \mu\text{s}$ and some other are arrested. For the excursions 1, 8 and 10, see the orange numbers in Fig. 4(a), the curve for $88 \mu\text{s}$ is above the curve for $93 \mu\text{s}$ and this, in turn, is above the curve for $98 \mu\text{s}$. This order of the $\hat{\varepsilon}_I - \bar{P}$ curves indicates that excursions 1, 8 and 10 do not grow for loading times greater than $88 \mu\text{s}$. For the excursions 2, 3, 6, 9 and 11, see the blue numbers in Fig. 4(a), the curve for $98 \mu\text{s}$ is above



(a)



(b)

Figure 3: Normalized maximum principal logarithmic strain $\hat{\epsilon}_I$ versus normalized angular position $\bar{P} = \frac{\Theta}{2\pi}$. Comparison between elasto-plastic and hyperelastic materials. (a) Applied velocity $V = 100 \text{ m/s}$. Loading time for the elasto-plastic material: $t = 98 \mu\text{s}$. Loading time for the hyperelastic material: $t = 73 \mu\text{s}$. (b) Applied velocity $V = 400 \text{ m/s}$. Loading time for the elasto-plastic material: $t = 48 \mu\text{s}$. Loading time for the hyperelastic material: $t = 36 \mu\text{s}$. The yellow dashed line, which indicates the value of $\hat{\epsilon}_I$ in the valleys corresponding to the elasto-plastic material, represents the accumulated plastic strain prior to full necking localization. The blue arrows indicate excursions of strain that have been arrested before forming a neck. (For interpretation of the references to colour in the text, the reader is referred to the web version of this article.)

the curve for $93 \mu s$ and this, in turn, is above the curve for $88 \mu s$. This shows that excursions 2, 3, 6, 9 and 11 grow within the time interval $88 - 98 \mu s$. It is important to note that the growth-rate of these excursions is significantly different. For instance, excursion 11 grows *faster* than excursion 2. The former increases from $\hat{\varepsilon}_I = 1.18$ to $\hat{\varepsilon}_I = 1.9$ within the time interval $88 - 98 \mu s$, and the later (only) from $\hat{\varepsilon}_I = 1.09$ to $\hat{\varepsilon}_I = 1.45$. For the excursions 4, 5 and 7, see the purple numbers in Fig. 4(a), the curve for $93 \mu s$ is above the curves for $88 \mu s$ and $98 \mu s$. This indicates that, while the excursions 4, 5 and 7 grow within the interval $88 - 93 \mu s$, they are arrested within the interval $93 - 98 \mu s$.

Fig. 4(b) shows results for the hyperelastic material and three loading times: $t = 63 \mu s$, $t = 68 \mu s$ and $t = 73 \mu s$. Note that the data corresponding to $t = 73 \mu s$ were already shown in Fig. 3(b). As in Fig. 4(a), the time interval covered by the data presented in Fig. 4(b) is $10 \mu s$. We observe a significant development of the localization pattern. The maximum value of $\hat{\varepsilon}_I$ (corresponding to excursion 7) turns from ≈ 0.978 at $t = 63 \mu s$, to ≈ 1.9 at $t = 73 \mu s$. Note that for the elasto-plastic material the increase of the maximum value of $\hat{\varepsilon}_I$ (which corresponds to excursion 11) is more modest, since it goes from ≈ 1.18 in the case of $t = 88 \mu s$ to ≈ 1.9 in the case of $t = 98 \mu s$, see Fig. 4(a). It becomes apparent that the localization pattern grows faster for the hyperelastic material than for the elasto-plastic material. Furthermore, referring to the order of the curves for $t = 63 \mu s$, $t = 68 \mu s$ and $t = 73 \mu s$ we observe that all the strain excursions grow during the investigated time interval. It is important to note that, as in the case of the elasto-plastic material, the growth-rate of the strain excursions varies from one to another. While, as mentioned before, excursion 7 is the one that grows faster, excursion 5 is the one that grows slower. Moreover, note also that all the valleys are being unloaded. Recall that unloading only ends when the strain goes to zero. As mentioned before, the rate of unloading of the valleys increases as the rate of growth of the surrounding strain excursions increases. This is because the elastic energy released from the valleys during their unloading is used to fuel the growth of the strain excursions, giving rise to a feedback process in which the faster the unloading of the valleys, the faster the development of the localization process (and vice versa). This process is hardly observed in the case of the elasto-plastic material, for which the elastic energy stored during the material deformation process is much more modest (the elastic strains are much smaller than the plastic strains). For elasto-plastic material, most of the external work input is plastically dissipated. In addition, the number of excursions which grow is gradually reduced with time, as shown in Fig. 4(a), in agreement with the finite element calculations reported by Zhou et al. (2006), who modelled the nucleation of multiple necks in rings made of uranium-6%-niobium. For the hyperelastic material, the growing of excursions may be significantly slowed down when the surrounding valleys are completely unloaded (i.e. when they have released all their stored elastic energy). But, still the external

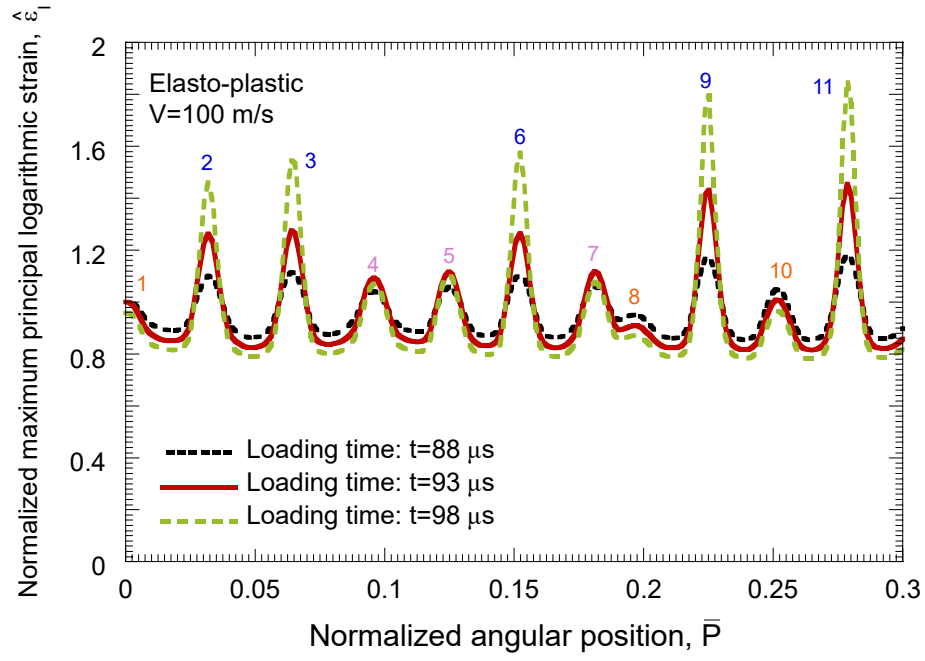
work may influence the evolution of necking.

Fig. 5 shows $\hat{\varepsilon}_I - \bar{P}$ curves for both materials investigated and different loading times. The difference with Fig. 4 is that the applied velocity has been increased to 400 m/s .

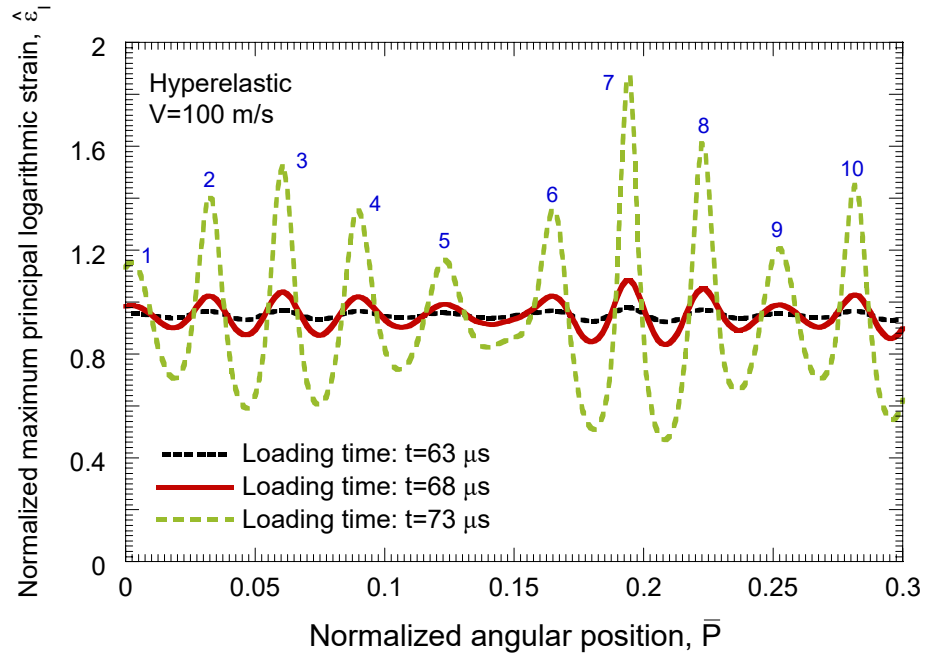
Fig. 5(a) shows results for the elasto-plastic material and three loading times: $t = 38 \text{ } \mu\text{s}$, $t = 43 \text{ } \mu\text{s}$ and $t = 48 \text{ } \mu\text{s}$. The data corresponding to $t = 48 \text{ } \mu\text{s}$ were already shown in Fig. 3(b). There are 15 excursions in strain. Relying on the order of the curves for the three loading times, we observe that 13 out of the 15 excursions grow within the time interval $38 - 48 \text{ } \mu\text{s}$. In comparison with the results presented in Fig. 4(a), the proportion of excursions which grow is greater, i.e. more necks develop. The unloading waves emanating from the necks play a less important role in the localization process at large loading velocities. It seems that the increase of inertia with the applied velocity leads to localization patterns formed by excursions of strain with more similar rates of growth. This is consistent, for instance, with the conclusions derived from the numerical work of Rodríguez-Martínez et al. (2013a).

Fig. 5(b) shows results for the hyperelastic material and three loading times: $t = 26 \text{ } \mu\text{s}$, $t = 31 \text{ } \mu\text{s}$ and $t = 36 \text{ } \mu\text{s}$. The data corresponding to $t = 36 \text{ } \mu\text{s}$ were already shown in Fig. 3(b). There are 17 excursions in strain and all of them grow during the time interval $26 - 36 \text{ } \mu\text{s}$. Note that excursion 4 is significantly less developed than the other excursions of strain and, even so, it develops and forms a neck (instead of being arrested). As in the $\hat{\varepsilon}_I - \bar{P}$ curve for $V = 100 \text{ m/s}$ presented in Fig. 4(b), not a single strain excursion is arrested. Recall that for the hyperelastic material arrested/unloaded means that the strain goes to zero.

Fig. 6 shows the number of necks nucleated in the whole ring N_N versus the applied velocity V for both materials. Irrespective of the material description considered, the number of necks increases non-linearly with the applied velocity featuring a concave-downward shape. There is a qualitative agreement between our numerical results and the experiments reported, for instance, in Altynova et al. (1996) and Zhang and Ravi-Chandar (2008), where rings made of different metallic ductile materials were investigated. Fig. 6 also shows that, for both materials, the number of necks is similar and proportional to $V^{0.3}$. Nevertheless, the hyperelastic rings show 10 to 15% more necks than the elasto-plastic rings. Based on the results presented in Figs. 4 and 5, this difference could be attributed to the fact that in the case of the hyperelastic rings all the excursions in strain develop into necks. On the contrary, for the elastic-plastic material some of the strain excursions do not reach the neck criterion we have used in this work (recall that we consider that a neck is formed when the strain ratio $\hat{\varepsilon}_I$ between the peak and the neighbouring valleys is greater than 1.1) and therefore they are not

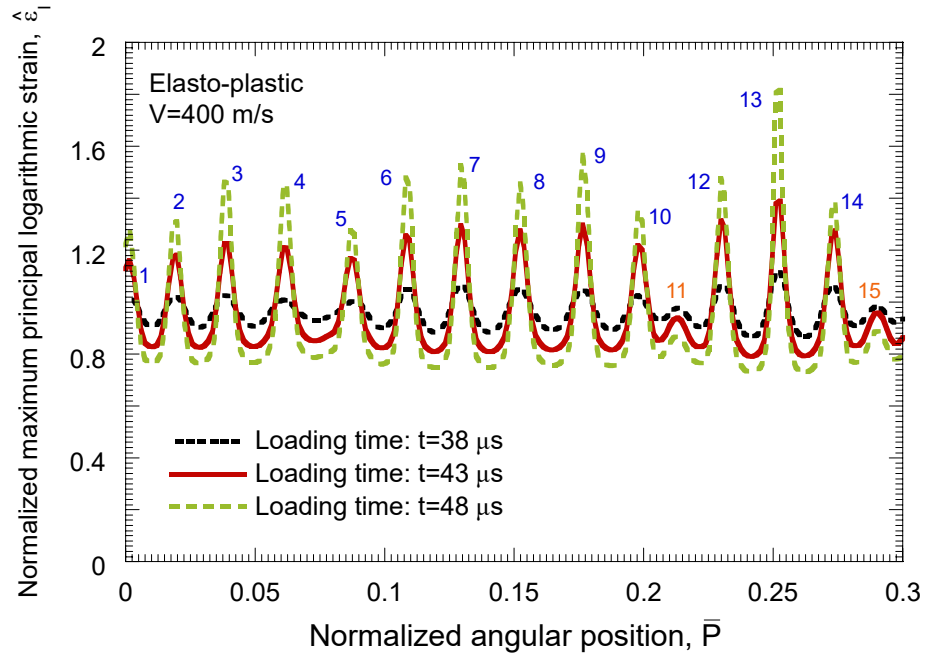


(a)

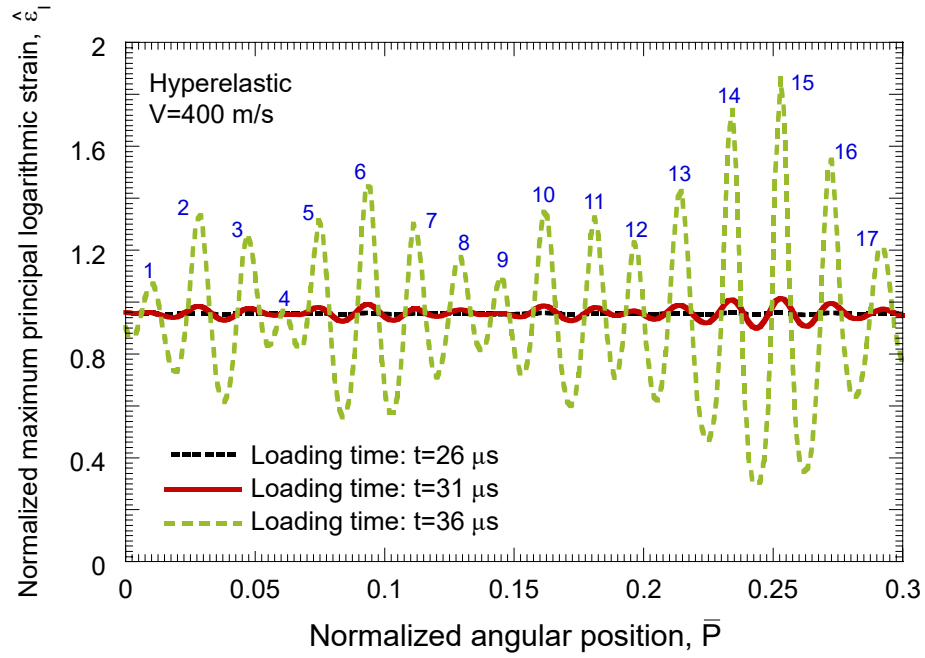


(b)

Figure 4: Normalized maximum principal logarithmic strain $\hat{\epsilon}_I$ versus normalized angular position $\bar{P} = \frac{\Theta}{2\pi}$. Applied velocity $V = 100$ m/s. (a) Elasto-plastic material. Three loading times are considered: $t = 88 \mu s$, $t = 93 \mu s$ and $t = 98 \mu s$. (b) Hyperelastic material. Three loading times are considered: $t = 63 \mu s$, $t = 68 \mu s$ and $t = 73 \mu s$. (For interpretation of the references to colour in the text, the reader is referred to the web version of this article.)



(a)



(b)

Figure 5: Normalized maximum principal logarithmic strain $\hat{\varepsilon}_I$ versus normalized angular position $\bar{P} = \frac{\Theta}{2\pi}$. Applied velocity $V = 400$ m/s. (a) Elasto-plastic material. Three loading times are considered: $t = 38 \mu s$, $t = 43 \mu s$ and $t = 48 \mu s$. (b) Hyperelastic material. Three loading times are considered: $t = 26 \mu s$, $t = 31 \mu s$ and $t = 36 \mu s$. (For interpretation of the references to colour in the text, the reader is referred to the web version of this article.)

included in the results presented in Fig. 6.

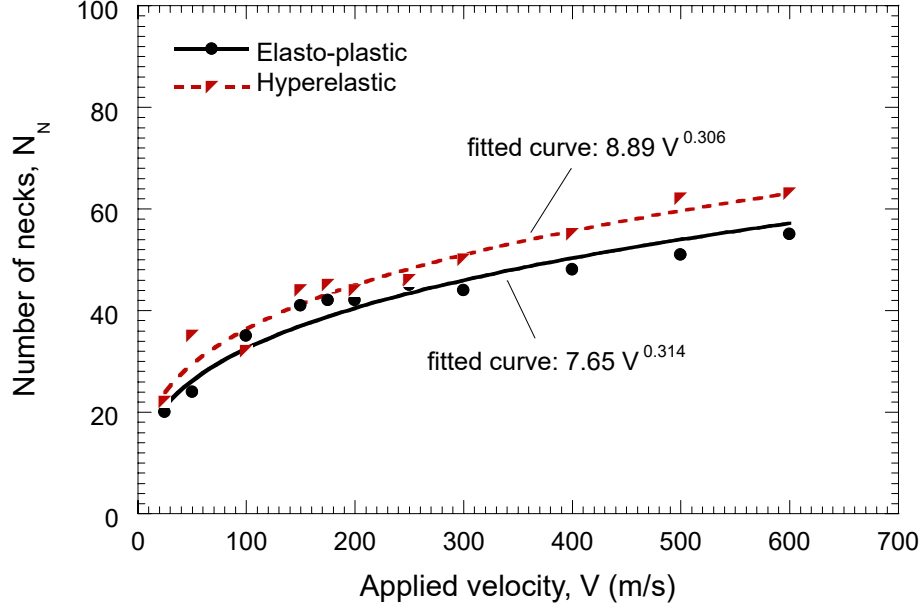


Figure 6: Number of necks N_N versus applied velocity V for elasto-plastic and hyperelastic materials. The number of necks increases with the applied velocity following a power-law relationship $N_N \propto V^{0.3}$ for both materials.

Fig. 7 shows the normalized average Lagrangian neck spacing L_n/e_0 versus the applied velocity V for the elasto-plastic and hyperelastic rings. Note that $\frac{L_n}{e_0} = \frac{2\pi R_o}{N_N e_0}$, where L_n is the average distance between two consecutive necks. Recall that e_0 and R_o are the initial thickness and initial outer radius of the ring, see Fig. 3. The neck spacing decreases with the applied velocity such that for both tested materials the $L_n/e_0 - V$ curve features a concave-upward shape such that $L_n/e_0 \propto V^{-0.3}$. This is a direct consequence of the results presented in Fig. 6, where it was shown that $N_N \propto V^{0.3}$. The $L_n/e_0 - V$ curve for the elasto-plastic material is slightly above the curve for the hyperelastic material for all the applied velocities since, as shown in Fig. 6, the number of necks in the elasto-plastic rings is smaller.

Moreover, the distance between consecutive necks is measured in the undeformed configuration, and normalized by the initial thickness of the ring, in order to calculate the standard deviation of the distribution of normalized neck spacings σ_u^{neck} . Fig. 8 shows σ_u^{neck} versus V for the elasto-plastic and the hyperelastic rings. The results for both materials are similar, the standard deviation of the distribution of normalized neck spacings decreases with the applied velocity featuring a concave-upward shape. This means that the distribution of neck sizes is more uniform as the applied velocity increases (i.e. as the strain rate increases). Following, for instance, Rodríguez-Martínez et al. (2013a), this behaviour can be attributed to the effect of inertia, which increases with strain rate, and promotes the development of necks with specific sizes (i.e. specific neck spacings).

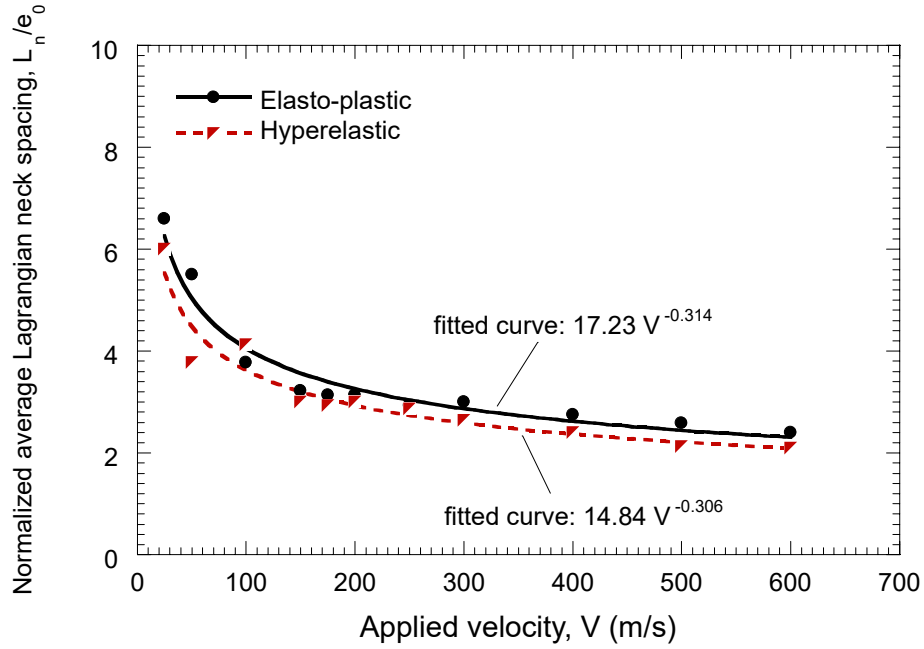


Figure 7: Normalized average Lagrangian neck spacing L_n/e_0 versus applied velocity V for elasto-plastic and hyperelastic materials. The normalized average Lagrangian neck spacing decreases with the applied velocity following a power-law relationship $L_n/e_0 \propto V^{-0.3}$ for both materials.

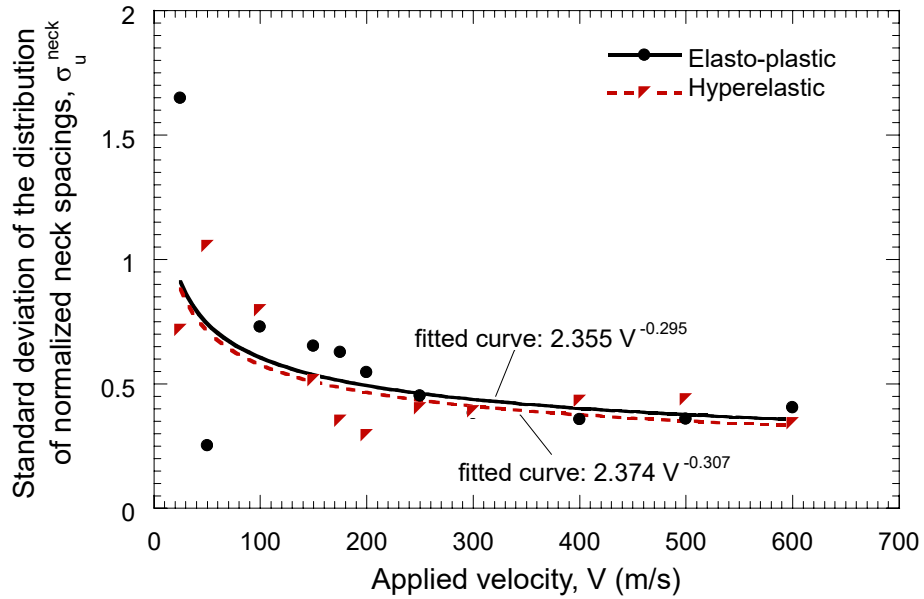


Figure 8: Standard deviation of the distribution of normalized neck spacings σ_u^{neck} versus the applied velocity V for elasto-plastic and hyperelastic materials. The standard deviation of the distribution of normalized neck spacings decreases with the applied velocity following a power-law relationship $\sigma_u^{neck} \propto V^{-0.3}$ for both materials.

The results presented so far have identified the differences in the mechanisms which control the development of the localization pattern in the elasto-plastic and the hyperelastic rings, [paying specific attention to the roles played by unloading waves, elastic stored energy and plastic dissipation](#). Next we pursue our analysis to investigate the fragmentation process.

Fig. 9 compares the number of fragments N_F obtained for the elasto-plastic and hyperelastic rings, for applied velocities ranging from 25 m/s to 600 m/s. For the elasto-plastic material, we assume that the failure occurs when the accumulated plastic strain reaches the failure strain $\bar{\varepsilon}_f = 1.5$, which corresponds to $E_f^{ep} = 2.68 \cdot 10^9 \text{ J/m}^3$, see equation (24). Recall from Section 3 that failure is assumed to occur in the hyperelastic material when the value of the strain energy density Ψ equals E_f^{ep} . Note that the failure criteria for both materials are based on an energy equivalence prior to failure. For the sake of simplicity, we just indicate in the figures the value of $\bar{\varepsilon}_f$, regardless of whether the results correspond to the elasto-plastic or the hyperelastic material. The number of fragments for the hyperelastic material is greater for the whole range of velocities investigated in this work. Since the number of necks in the hyperelastic and the elasto-plastic rings is not much different (see Fig. 6), it is obvious that the number of necks that produce complete fractures and fragments is greater in the hyperelastic specimens.

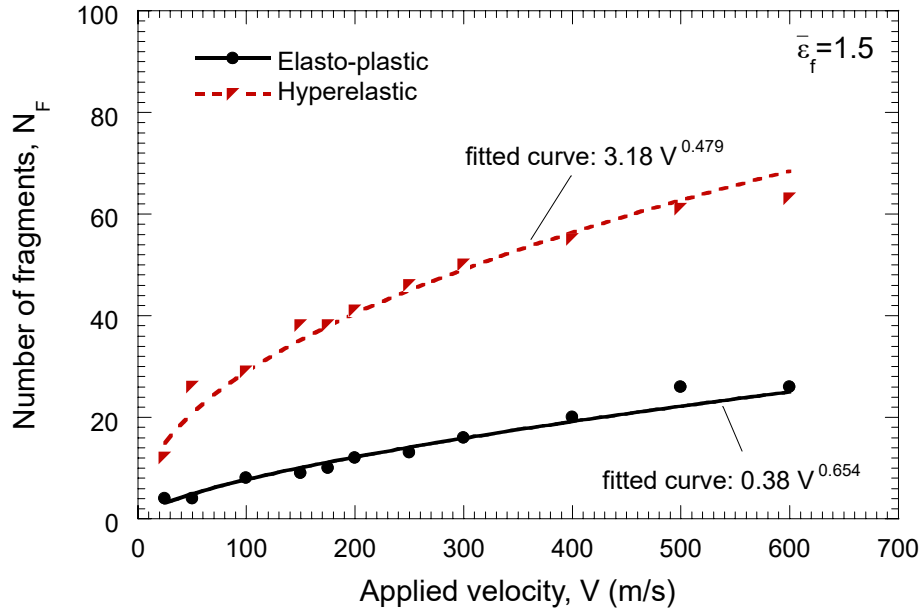


Figure 9: Number of fragments N_F versus applied velocity V for elasto-plastic and hyperelastic materials. Failure strain for the elasto-plastic material $\bar{\varepsilon}_f = 1.5$, which corresponds to $E_f^{ep} = 2.68 \cdot 10^9 \text{ J/m}^3$.

The differences in the fragmentation behaviors of elasto-plastic and hyperelastic rings is further illustrated

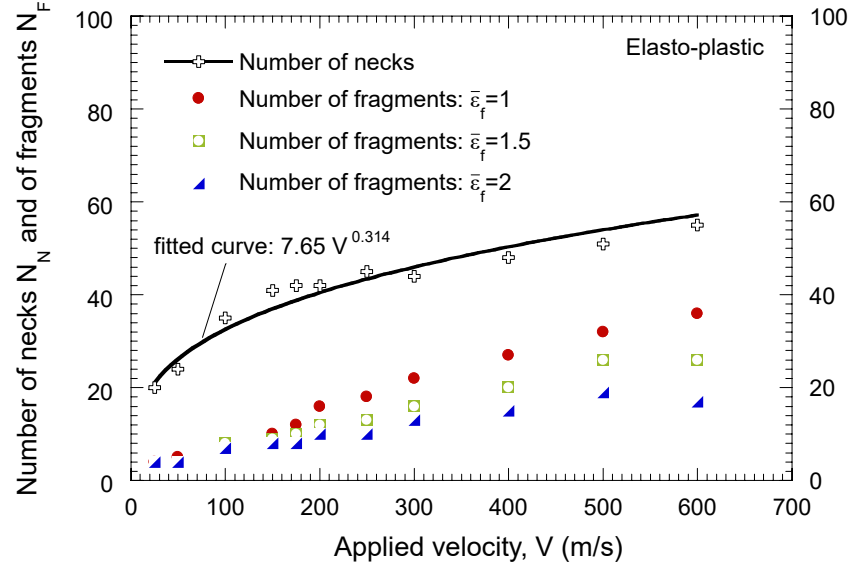
in Fig. 10, which compares the number of necks N_N and fragments N_F for both materials. Namely, Fig. 10(a) shows the results for the elasto-plastic material, and Fig. 10(b) for the hyperelastic one. The results are presented for various velocities ranging from 25 m/s to 600 m/s. Three different equivalent failure strains are considered in the calculations: $\bar{\varepsilon}_f = 1$, $\bar{\varepsilon}_f = 1.5$ and $\bar{\varepsilon}_f = 2$. These failure strains correspond to failure strain energies of $1.64 \cdot 10^9$, $2.68 \cdot 10^9$ and $3.81 \cdot 10^9$ J/m³, respectively.

For the elasto-plastic material, Fig. 10(a) shows that the number of fragments is smaller than the number of necks for the whole range of applied velocities considered. The greater the value of $\bar{\varepsilon}_f$, the greater the difference between necks and fragments. Indeed, the increase of the failure strain results in more arrested necks. This is consistent with the results previously presented in Figs. 4(a) and 5(a), which showed that the number of growing necks is gradually reduced with time. As the failure strain increases, the time that elapses from the formation of the neck until it meets the fracture criterion is greater, and therefore the chances for the neck to get arrested before fracture are higher. In other words, the release waves emanating from the necks have more time to unload the neighbouring sections of the specimen. It is also shown that the gap between the number of necks and fragments decreases with increasing V . We have run additional finite element calculations (not shown here for the sake of brevity) to check that for sufficiently high applied velocities (≈ 1200 m/s for $\bar{\varepsilon}_f = 1.5$) most of the necks incepted develop into fractures (64 necks and 56 fractures, being the ratio fragments-to-necks $\approx 90\%$), in agreement with the numerical results shown in Rodríguez-Martínez et al. (2013a). *Note that for $V = 600$ m/s, and $\bar{\varepsilon}_f = 1.5$, the ratio is only $\approx 48\%$.* The fact that as the applied velocity increases the proportion of necks that produces fractures increases is attributed to inertia effects, which tend to homogenize the size of the necks (see Fig. 7) and their growth-rates (see Fig. 5(a)). *Note that, since the material is rate insensitive, the increase in the proportion of necks that produces fractures cannot be attributed to viscous regularization.* On the other hand, by increasing the applied velocity, the time that elapses from the formation of the neck until the fracture criterion is met decreases, which also *reduces* the chances for the neck to get arrested before fracture since the release waves will unload smaller portions of the ring. Fig. 11 shows a sequence of contour plots of maximum principal logarithmic strain ε_I which illustrate the processes of homogeneous deformation, strain localization and fragmentation in the ring expanded at $V = 100$ m/s. All the isocontours have the same colour coding such that maximum principal logarithmic strains ranging from 0.3 to 1 correlate with a colour scale that goes from blue to red. Maximum principal logarithmic strains below 0.3 remain blue and above 1 remain red. Fig. 11(a) corresponds to the loading time $t = 78$ μ s, for which the deformation in the ring only shows small variations in ε_I (from 0.392 to 0.405) which are not visible due to the colour scale used in the contour plots. Fig. 11(b), which corresponds to $t = 84$ μ s, shows the onset of the localization process. The sequence of dark blue and

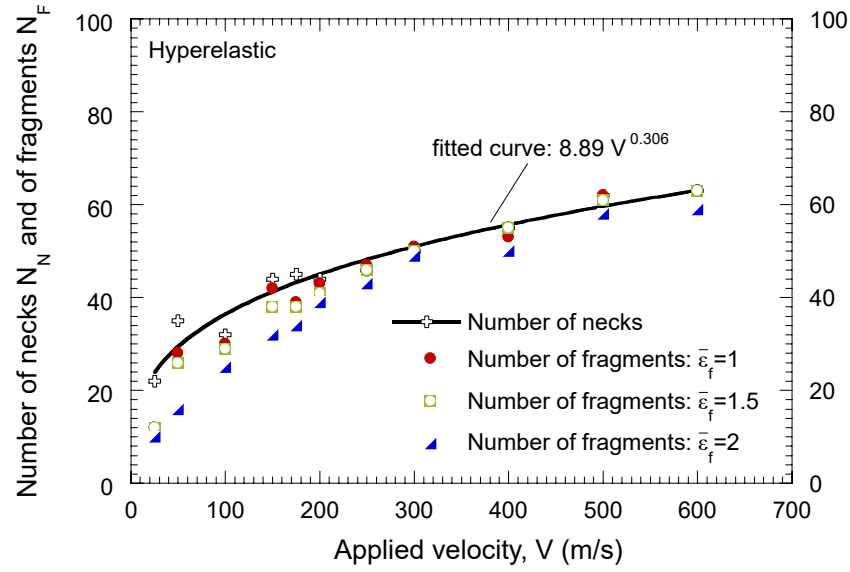
light blue zones indicate the formation of strain gradients in the sample. Figs. 11(c)-(d) show contours for $t = 93 \mu s$ and $t = 98 \mu s$. For these loading times, the necking pattern is already formed, as previously shown in Fig. 4(a). The colour coding also reveals that some necks (in red) are more developed than others (in yellow and green). Fig. 11(e) shows contours for $t = 106 \mu s$, which corresponds to the onset of the fragmentation. Four fractures, which occur roughly at the same time, are indicated in the plot. The fracture sites release stress waves which unload the neighbouring sections of the ring and hinder further development of nearby necks. Altogether, some necks can be refrained by fast growing neighbour necks or arrested by unloading waves emanating from fracture sites, but, there are still several necks which keep on growing for loading times greater than $106 \mu s$. For instance, some necks in Fig. 11(f) are more developed than in Fig. 11(e). The processes of strain localization and fragmentation continue until, for $t = 109 \mu s$, the fragmentation is completed. Eight fractures are counted in Fig. 11(g).

For the hyperelastic material, Fig. 10(b) shows that the number of fragments is smaller than the number of necks only for the lower applied velocities. If $V \geq 250 \text{ m/s}$ the number of fragments roughly equals the number of necks, and $\bar{\varepsilon}_f$ plays a minor role in the number of fractures which form in the ring. In comparison with the elasto-plastic material, which requires an applied velocity of $\approx 1200 \text{ m/s}$ so that the proportion of necks that develop into fragments is $\approx 90\%$, the hyperelastic material promotes that most of the nucleated necks develop into fractures for much lower applied velocities. **Namely, the proportion of necks that leads to fracture sites reaches $\approx 90\%$ for $V = 200 \text{ m/s}$.** As mentioned before, for the hyperelastic material, during the homogeneous deformation process, before the necks are formed, the mechanical work is stored in the form of elastic energy. Once the necking pattern is formed, the sections of the ring which unload release the elastic stored energy which is then used to feed the necks so that they all grow. The only necks that do not reach fracture are those arrested due to the unloading waves emanating from fractures. The localization and fragmentation processes are illustrated in Fig. 12 which shows a sequence of contour plots of maximum principal logarithmic strain ε_I for different loading times, for the ring expanded at $V = 100 \text{ m/s}$. The colour coding of the isocontours is the one used in Fig. 11. In Fig. 12(a), which corresponds to $t = 63 \mu s$, the strain heterogeneity in the sample is very modest and not visible in the contours because of the colour scale used. Results for this loading time were also shown in Fig. 4(b). The maximum value of ε_I is 0.342 and the minimum 0.323. Fig. 12(b) shows contours for $t = 68 \mu s$. There is a sequence of light and dark blue zones which correspond to regions subjected to loading, and regions which are unloading, respectively. Results for this loading time were also shown in Fig. 4(b). The necking pattern that emerges in the ring is easily identifiable in Fig. 12(c), which shows contours for $t = 73 \mu s$. Results for this loading time were also shown in Fig. 4(b). Shortly after, for $t = 76 \mu s$, some

necks lead to fractures, as shown in Fig. 12(d). When fracture occurs, the neighbouring sections of the ring are subjected to potent release waves, that come to compress the material, and preclude the development of the necks which are located in these regions. These are the only necks that do not produce fractures. All the necks which are not located in these regions keep on growing and new fractures appear in the ring for $t = 78 \mu s$ and $t = 80 \mu s$, as shown in Figs 12(e)-(f). The fragmentation is completed for $t = 82 \mu s$ with a total of 29 fractures in the sample, 21 more than in the case of the elasto-plastic material. Altogether, it appears clearly that: (i) similar results have been obtained for the onset of multiple necking for rings made up of elasto-plastic material and a comparison hyperelastic material, (ii) differences are emerging during the evolution of the localization process and (iii) a clear gap between results appears when fragmentation is triggered.



(a)



(b)

Figure 10: Number of necks N_N and of fragments of N_F versus the applied velocity V . The number of fragments obtained from numerical calculations performed with three different failure strains is shown: $\bar{\varepsilon}_f = 1$, $\bar{\varepsilon}_f = 1.5$ and $\bar{\varepsilon}_f = 2$. (a) Elasto-plastic material. (b) Hyperelastic material. The number of fragments in the elasto-plastic rings is smaller than in the hyperelastic ones.

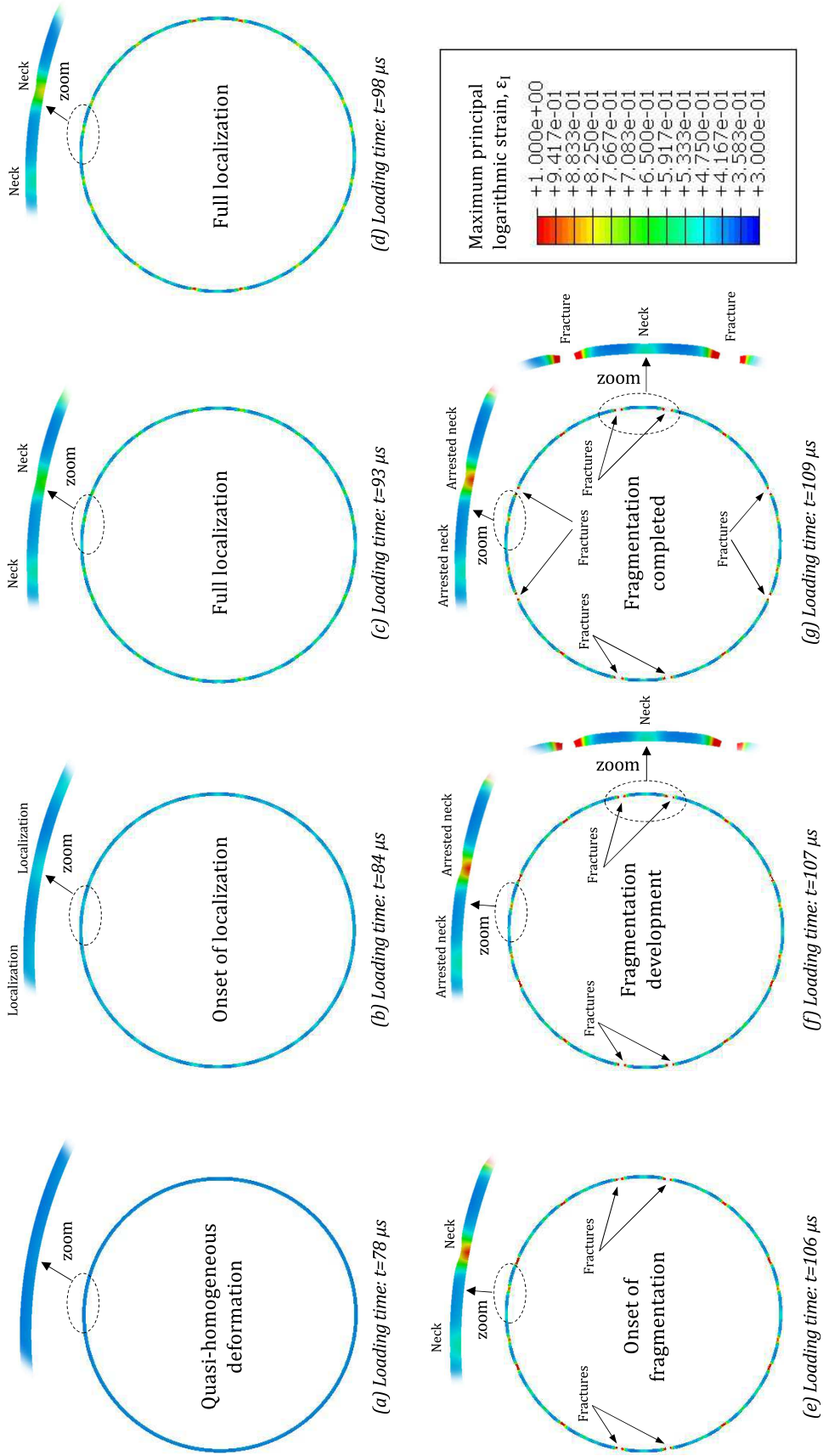


Figure 11: Elasto-plastic material. Contours of maximum principal logarithmic strain ε_I for seven different loading times: (a) $t = 78 \mu s$, (b) $t = 84 \mu s$, (c) $t = 93 \mu s$, (d) $t = 98 \mu s$, (e) $t = 106 \mu s$, (f) $t = 107 \mu s$, (g) $t = 109 \mu s$. The applied velocity is $V = 100 \text{ m/s}$ and the failure strain is $\bar{\varepsilon}_f = 1.5$. (For interpretation of the references to colour in the text, the reader is referred to the web version of this article.)

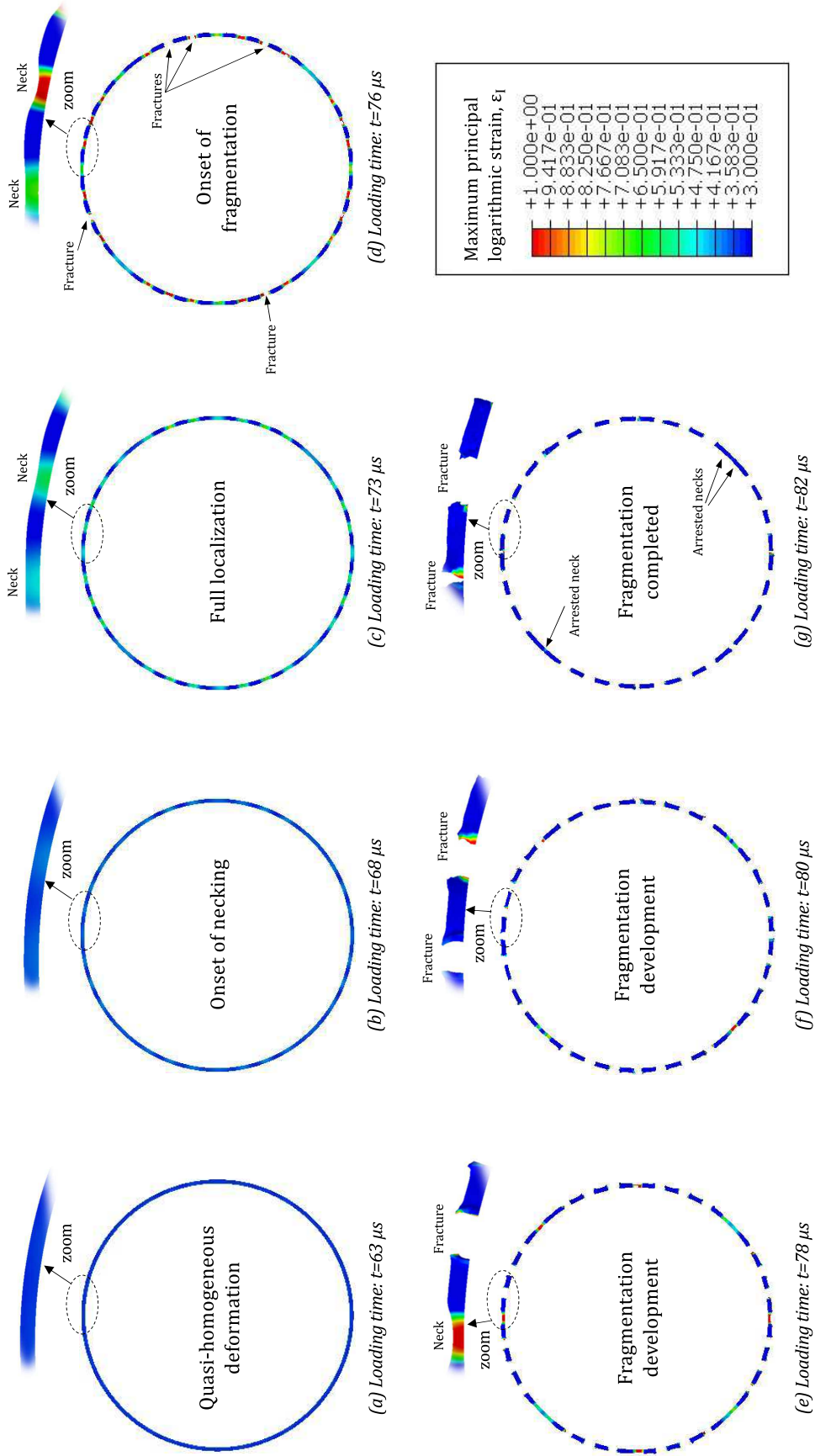


Figure 12: Hyperelastic material. Contours of maximum principal logarithmic strain ϵ_I for seven different loading times: (a) $t = 63 \mu s$, (b) $t = 68 \mu s$, (c) $t = 73 \mu s$, (d) $t = 76 \mu s$, (e) $t = 78 \mu s$, (f) $t = 80 \mu s$, (g) $t = 82 \mu s$. The applied velocity is $V = 100 \text{ m/s}$ and failure strain is $\bar{\epsilon}_f = 1.5$. (For interpretation of the references to colour in the text, the reader is referred to the web version of this article.)

5. Conclusion

In this work we have carried out a comparative study of the necking and fragmentation behaviours of elasto-plastic and hyperelastic rings subjected to dynamic loading. For that purpose, we have conducted finite element simulations in ABAQUS/Explicit (2013) for expansion velocities that range between 25 m/s and 600 m/s . The elasto-plastic material and the comparison hyperelastic material are modelled with idealized constitutive equations which provide nearly the same stress-strain response under monotonic uniaxial tensile loading, and fracture is assumed to occur at the same level of deformation energy for both materials. The main findings of this work, which aims to shed light into the roles of unloading waves, elastic stored energy and plastic dissipation in the multiple localization and fragmentation behaviours of ductile materials, are summarized below:

- The number of necks nucleated is similar for both materials, for the whole range of applied velocities. The distributions of neck spacing are also very similar. Notably, the standard deviations of neck spacing are much the same and are decreasing functions of the applied velocity. The number and size of the necks is mostly determined by the loading response of the material.
- In the elasto-plastic rings, some of the nucleated necks are arrested during the localization process due to the stress release waves that travel the ring once localization starts. Since the growth-rate and spacing of the necks becomes more regular as inertia effects increase, the proportion of necks arrested decreases as the applied velocity increases. In the hyperelastic rings, irrespective of the applied velocity, none of the nucleated necks is arrested during the localization regime prior to the fracturing process. The elastic energy released from the unloading sections of the specimen is used to fuel the growth of the necks. Hence, the necking pattern grows faster in the hyperelastic rings than in the elasto-plastic ones. The unloading response of the material plays a key role in the development of the necking pattern.
- The proportion of necks that develop into fractures depends on the material and the applied velocity. In the hyperelastic ring, most of the necks lead to fragments, since necks are not arrested during the localization process preceding fragmentation. The only necks that do not lead to fracture are those arrested, after the onset of fracturing, by the stress release waves emanating from sections of the ring that fracture first. For velocities above 250 m/s , since the hyperelastic necks grow very fast, these release waves do not have time to affect the fragmentation, and the number of fragments roughly equals the number of necks. In the elasto-plastic rings, for the applied velocities investigated in this work, the number of fragments is significantly smaller than the number of incepted necks. Since the localization

pattern develops slower than for the hyperelastic material, the stress waves released from early fractures have time to arrest additional necks to those that were already arrested during the localization process. Nevertheless, as the expansion velocity increases, the proportion of necks that triggers fracture increases.

Acknowledgements

AM and JARM acknowledge the support by the French State through the program Investment in the future operated by the *National Research Agency* (ANR) and referenced by ANR-11-LABX-0008-01 (LabEx DAMAS).

AVR acknowledges the financial support obtained from the University Carlos III of Madrid through the programme *Ayudas para la movilidad – Convocatoria 2017*.

The research leading to these results has received funding from the European Research Council (ERC) under the European Union’s Horizon 2020 research and innovation programme. Project PURPOSE, grant agreement 758056.

References

- ABAQUS/Explicit, 2013. Abaqus Explicit v6.13 User’s Manual, version 6.13 Edition. ABAQUS Inc., Richmond, USA.
- Altynova, M., Hu, X., Daehn, G. S., 1996. Increased ductility in high velocity electromagnetic ring expansion. *Metall Trans A* 27, 1837–1844.
- Becker, R., 2002. Ring fragmentation predictions using the Gurson model with material stability conditions as failure criterion. *International Journal of Solids and Structures* 39, 3555–3580.
- Bergstrom, J., 2015. *Mechanics of Solid Polymers*, 1st Edition. Elsevier, Mineola.
- Cliche, N., Ravi-Chandar, K., 2018. Dynamic strain localization in magnesium alloy AZ31B-O. *Mechanics of Materials* 116, 189–201.
- El Maï, S., Mercier, S., Petit, J., Molinari, A., 2014. An extension of the linear stability analysis for the prediction of multiple necking during dynamic extension of round bar. *International Journal of Solids and Structures* 51, 3491–3507.

- Fressengeas, C., Molinari, A., 1994. Fragmentation of rapidly stretching sheets. *European Journal of Mechanics A/Solids* 13, 251–268.
- Gough, J., Gregory, I., Muhr, A., 1999. *Determination of Constitutive Equations for Vulcanized Rubber*. Professional Engineering Publishing, London.
- Grady, D., 2002. Fragmentation of expanding cylinders and the statistical theory of N. F. Mott. In: Furnish, M. D., Thadhani, N. N., Horie, Y. (Eds.), *Shock Compression of Condensed Matter - 2001*. . American Institute of Physics, pp. 799–802.
- Grady, D., 2006. *Fragmentation of rings and shells the legacy of N. F. Mott*, 1st Edition. Springer-Verlag Berlin Heidelberg.
- Grady, D. E., Kipp, M. E., Benson, D. A., 1984. Energy and statistical effects in the dynamic fragmentation of metal rings. In: Harding, J. (Ed.), *Mechanical properties at high strain rates*. . Institute of Physics, Bristol, pp. 315–320.
- Grady, D. E., Olsen, M. L., 2003. A statistics and energy based theory of dynamic fragmentation. *International Journal of Impact Engineering* 29, 293–306.
- Hutchinson, J. W., Neale, K. W., 1983. Neck propagation. *Journal of the Mechanics and Physics of Solids* 31, 405–426.
- Kipp, M. E., Grady, D. E., 1985. Dynamic fracture growth and interaction in one dimension. *Journal of the Mechanics and Physics of Solids* 33, 399–415.
- Marlow, R., 2003. A general first-invariant hyperelastic constitutive model. *Proceedings of the Third European Conference on Constitutive Models for Rubber*, Busfield and Muhr, London, pp. 157–160.
- Mercier, S., Molinari, A., 2003. Predictions of bifurcations and instabilities during dynamic extensions. *International Journal of Solids and Structures* 40, 1995–2016.
- Mercier, S., Molinari, A., 2004. Analysis of multiple necking in rings under rapid radial expansion. *International Journal of Impact Engineering* 30, 403–419.
- Mott, N. F., 1947. Fragmentation of shell cases. In: . *Series A. Proceedings of the Royal Society, London*, pp. 300–308.

- Needleman, A., 1991. The effect of material inertia on neck development. In: Yang, W.H. (Ed.), Topics in Plasticity. AM Press, Ann Arbor, MI, 151–160.
- Niordson, F. L., 1965. A unit for testing materials at high strain rates. *Experimental Mechanics* 5, 29–32.
- N’souglo, K. E., Srivastava, A., Osovski, S., Rodríguez-Martínez, J. A., 2018. Random distributions of material defects trigger regular necking patterns at high strain rates. *Proceedings of the Royal Society A: Mathematical, Physical and Engineering Sciences* 474, 20170575.
- Ogden, R. W., 1997. *Non-Linear Elastic Deformations*, 1st Edition. Dover Publications, Mineola.
- Ravi-Chandar, K., Triantafyllidis, N., 2015. Dynamic stability of a bar under high loading rate: Response to local perturbations. *International Journal of Solids and Structures* 58, 301–308.
- Rodríguez-Martínez, J. A., Molinari, A., Zaera, R., Vadillo, G., Fernández-Sáez, J., 2017. The critical neck spacing in ductile plates subjected to dynamic biaxial loading: On the interplay between loading path and inertia effects. *International Journal of Solids and Structures* 108, 74–84.
- Rodríguez-Martínez, J. A., Vadillo, G., Fernández-Sáez, J., Molinari, A., 2013a. Identification of the critical wavelength responsible for the fragmentation of ductile rings expanding at very high strain rates. *Journal of the Mechanics and Physics of Solids* 61, 1357–1376.
- Rodríguez-Martínez, J. A., Vadillo, G., Zaera, R., Fernández-Sáez, J., 2013b. On the complete extinction of selected imperfection wavelengths in dynamically expanded ductile rings. *Mechanics of Materials* 60, 107–120.
- Rodríguez-Martínez, J. A., Vadillo, G., Zaera, R., Fernández-Sáez, J., Rittel, D., 2015. An analysis of microstructural and thermal softening effects in dynamic necking. *Mechanics of Materials* 80B, 298–310.
- Rusinek, A., Zaera, R., 2007. Finite element simulation of steel ring fragmentation under radial expansion. *International Journal of Impact Engineering* 34, 799–822.
- Treolar, L. R. G., 1944. Stress–strain data for vulcanised rubber under various types of deformation. *Transactions of the Faraday Society* 40, 59–70.
- Vadillo, G., Rodríguez-Martínez, J. A., Fernández-Sáez, J., 2012. On the interplay between strain rate and strain rate sensitivity on flow localization in the dynamic expansion of ductile rings. *International Journal of Solids and Structures* 49, 481–491.

- Vaz-Romero, A., Rodríguez-Martínez, J. A., Mercier, S., Molinari, A., 2017. Multiple necking pattern in nonlinear elastic bars subjected to dynamic stretching: The role of defects and inertia. *International Journal of Solids and Structures* 125, 232–243.
- Xue, Z., Vaziri, A., Hutchinson, J. W., 2008. Material aspects of dynamic neck retardation. *Journal of the Mechanics and Physics of Solids* 56, 93–113.
- Zhang, H., Ravi-Chandar, K., 2006. On the dynamics of necking and fragmentation - I. Real-time and post-mortem observations in Al 6061-O. *International Journal of Fracture* 142, 183–217.
- Zhang, H., Ravi-Chandar, K., 2008. On the dynamics of necking and fragmentation - II. Effect of material properties geometrical constraints and absolute size. *International Journal of Fracture* 150, 3–36.
- Zhang, H., Ravi-Chandar, K., 2010. On the dynamics of localization and fragmentation-IV. Expansion of Al 6061-O tubes. *International Journal of Fracture* 163, 41–65.
- Zhou, F., Molinari, J. F., Ramesh, K. T., 2006. An elasto-visco-plastic analysis of ductile expanding ring. *International Journal of Impact Engineering* 33, 880–891.